HHS Public Access

Author manuscript

Nano Lett. Author manuscript; available in PMC 2024 January 16.

Published in final edited form as:

Nano Lett. 2023 March 08; 23(5): 1717–1725. doi:10.1021/acs.nanolett.2c04404.

First Superferromagnetic Remanence Characterization and Scan Optimization for Super-Resolution Magnetic Particle Imaging

K. L. Barry Fung,
UC Berkeley-UCSF Graduate Group in Bioengineering, University of California Berkeley and University of California San Francisco

Caylin Colson,
UC Berkeley-UCSF Graduate Group in Bioengineering, University of California Berkeley and University of California San Francisco

Jacob Bryan,
Department of Bioengineering, University of California Berkeley, Berkeley, California 94720, United States

Chinmoy Saayujya,
Department of Electrical Engineering and Computer Sciences, University of California Berkeley, Berkeley, California 94720, United States

Javier Mokkarala-Lopez,
Department of Bioengineering, University of California Berkeley, Berkeley, California 94720, United States

Allison Hartley,
Department of Bioengineering, University of California Berkeley, Berkeley, California 94720, United States

Khadija Yousuf,
Department of Bioengineering, University of California Berkeley, Berkeley, California 94720, United States

Renesmee Kuo,

Corresponding Author: K. L. Barry Fung − UC Berkeley-UCSF Graduate Group in Bioengineering, University of California Berkeley and University of California San Francisco, https://bioegrad.berkeley.edu/; barry.kl.fung@berkeley.edu.

Author Contributions

K.L.B.F. and S.M.C. conceptualized the remanence models and initial remanence experiments. K.L.B.F. developed, executed, and analyzed the followup experiments. J.B. carried out sonication experiments. K.L.B.F. and C.C. acquired the SFMIO images. R.K. performed iron quantification. K.L.B.F., C.S., and Y.L. assessed remanence models. C.C., C.S., Y.L., B.D.F., P.C., and S.M.C. refined methodology. J.B., J.M.-L., A.H., and K.Y. synthesized SFMIOs. K.L.B.F. prepared the draft and figures. All authors reviewed and approved the final draft.

ASSOCIATED CONTENT

Supporting Information

The Supporting Information is available free of charge at https://pubs.acs.org/doi/10.1021/acs.nanolett.2c04404.

Supplemental Figure 1: MPI images of the phantoms in Figure 1A–C, normalized to peak intraimage signal. Supplemental Figure 2: Remanence decay vs B_{SS} for $M_{SFMIO} > 0$ (complementary to Figure C). Supplemental Figure 3: Slew-normalized PSFs for Figure 5A's SFMIOs and theoretical coercivity losses in MPI scans. Supplemental Figure 4: Characteristic TEM images of the SFMIOs used in Figure 5A (PDF)

The authors declare the following competing financial interest(s): Dr. Steven M. Conolly is a co-founder of an MPI company, Magnetic Insight, and holds stock in this company. The authors declare no other conflict of interest.

Department of Bioengineering, University of California Berkeley, Berkeley, California 94720, United States

Yao Lu,
Department of Bioengineering, University of California Berkeley, Berkeley, California 94720, United States

Benjamin D. Fellows,
Department of Bioengineering, University of California Berkeley, Berkeley, California 94720, United States

Prashant Chandrasekharan,
Department of Bioengineering, University of California Berkeley, Berkeley, California 94720, United States

Steven M. Conolly
Department of Bioengineering, University of California Berkeley, Berkeley, California 94720, United States; Department of Electrical Engineering and Computer Sciences, University of California Berkeley, Berkeley, California 94720, United States

Abstract

Magnetic particle imaging (MPI) is a sensitive, high-contrast tracer modality that images superparamagnetic iron oxide nanoparticles, enabling radiation-free theranostic imaging. MPI resolution is currently limited by scanner and particle constraints. Recent tracers have experimentally shown 10 × resolution and signal improvements with dramatically sharper M–H curves. Experiments show a dependence on interparticle interactions, conforming to literature definitions of superferromagnetism. We thus call our tracers superferromagnetic iron oxide nanoparticles (SFMIOs). While SFMIOs provide excellent signal and resolution, they exhibit hysteresis with non-negligible remanence and coercivity. We provide the first quantitative measurements of SFMIO remanence decay and reformation using a novel multiecho pulse sequence. We characterize MPI scanning with remanence decay and coercivity and describe an SNR-optimized pulse sequence for SFMIOs under human electromagnetic safety limitations. The resolution from SFMIOs could enable clinical MPI with 10 × reduced scanner selection fields, reducing hardware costs by up to 100 ×.

Graphical Abstract

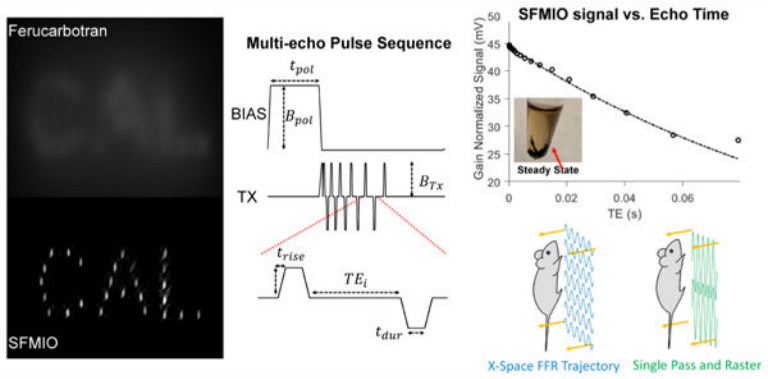

Keywords

Magnetic particle imaging; superferromagnetism; superparamagnetic iron oxide; superresolution

Magnetic particle imaging (MPI) is an emerging tracer modality[1,2] that directly images the magnetization of superparamagnetic iron oxide nanoparticles (SPIOs) with a positive, linear contrast. First described by Gleich and Weizenecker in 2005,[1] MPI leverages the nonlinear magnetic response of SPIOs to localize the SPIOs and generate an image proportional to tracer concentration.

Iron oxide nanoparticle tracers were first introduced to magnetic resonance imaging (MRI) by Lauterbur's group in 1986.[3] Superparamagnetic iron oxide nanoparticles (SPIOs) have been traditionally used in MRI, primarily as a T2*-weighted contrast agent. High concentrations of SPIOs produce dark signals on T2*-MRI, which radiologists term "negative contrast," and different SPIO formulations can yield varied targeting and contrast.[4] Unfortunately, it is challenging to distinguish a dark T2* signal from a naturally dark signal (e.g., the MRI signal in the lungs, bones, cartilage). Hence, quantitative measurements with T2*-SPIOs remain challenging.[5–9] An exception here is liver MRI, where SPIOs are preferentially taken up by healthy liver tissue, leaving dysfunctional tissue (e.g., function lost due to liver cancer) with a bright signal.[10] In addition, USPIOs can serve as a T1-shortening agent, although this can yield poor image quality due to the aforementioned T2*-shortening effects.

In comparison, the MPI signal depends on the SPIO's nonlinear magnetic response. Unlike human tissue, which remains linear[7] well above 3 T, SPIOs reach a saturation magnetization at low applied fields[11] (typically ~ 6 mT). This nonlinear saturation yields the harmonics in MPI signals[12] and allows for positive-contrast detection of SPIOs with no background signal from tissues.[13] Moreover, the MPI signal is robust to magnetic field inhomogeneities (5% field variations are well tolerated[14] vs 10 ppm for MRI) and has minimal attenuation from tissue depth given its relatively low frequencies ($\max(f_{sig}) \ll 10$ MHz),[13] making MPI suitable for imaging the entire body. Given these upsides, MPI shows promise in imaging applications previously dominated by nuclear medicine, like pulmonary embolism detection,[15–17] cancer,[18] gut bleed,[19] and white blood cell (neutrophil) imaging of cancer,[20]

infection, and bone marrow function.[21] MPI also shows promise in theranostics, assisting in targeted drug delivery,[22] cell therapy monitoring,[23,24] and magnetic hyperthermia treatment.[25–27]

However, despite its excellent safety profile and proven *in vivo* applications, MPI still faces a hurdle to clinical translation due to its resolution. MPI's resolution is roughly 1 mm[12,28] in preclinical scanners with intense 6.3–7 T/m selection fields,[19,29,30] as compared to $< 500\ \mu$m in other preclinical tracer modalities.[31] While these resolutions are comparable, scaling up magnetic systems is incredibly expensive, with human versions of preclinical MPI scanners projected to require field strengths equivalent to multimillion dollar 7 T MRIs. This would be an *order* of magnitude more expensive than positron emission tomography and X-ray computed tomography scanners. As such, MPI is in need of fundamental (and cost-effective) improvements to the resolution.

Improving MPI's fundamental resolution requires improving the SPIO's magnetic response or the scanner's gradient strength. Since MPI utilizes inductive measurements of magnetization, its point spread function (PSF) is proportional to the derivative of the Langevin function,[2] convolved with the SPIO's magnetic relaxation behavior[32] in time. The resulting resolution, measured as full-width at half-max (fwhm), is approximately

$$\Delta x \approx \frac{1}{G}\left(\Delta B + \tau \frac{\mathrm{d}B_{app}}{\mathrm{d}t}\right) \tag{1}$$

where ΔB is the width of the Langevin's magnetic transition in T, τ is the magnetic relaxation time constant in s, B_{app} is the applied magnetic field during a scan (in T), $\mathrm{d}B_{app}/\mathrm{d}t$ is the slew rate of the applied field (in T/s), and G is the gradient in T/m. In MPI, the relaxation of a magnetic particle can be modeled as an exponential decay with time constant τ.[32] Based on the scanner's magnetic slew rate, the ideal magnetic resolution ΔB is thus blurred by the slew rate multiplied by signal decay constant (i.e., τ), as in eq 1.

Of the two approaches to improving MPI resolution, scaling gradient strength is costly and can require superconducting magnets costing millions.[33] As a result, recent work has focused on modifying SPIO behavior. Notably, the magnetic transition scales inversely with magnetic volume (i.e., $\Delta B \propto d_{\mathrm{mag}}^{-3}$), while the relaxation time scales with hydrodynamic volume and to the natural exponent of the magnetic volume $\tau \propto d_h^3$, $\exp(d_{\mathrm{mag}}^3)$.[34] The net effect results in a reduction of sensitivity and resolution of the MPI system above a magnetic particle diameter threshold (dubbed the "relaxation wall"[28]). Empirically, this threshold was found to be 25 nm for single core magnetite particles (at 20 mT amplitude and 20 kHz excitation). However, optimal tracers still only had effective resolutions of ~ 1 mm.[12,28] Strategies modifying acquisition waveforms[25,35,36] and reconstruction methods[37,38] have provided methods for bypassing the relaxation wall resolution limit, but each method suffers from long scan times, lower sensitivity, high SNR requirements, or limiting algorithmic priors.

Recently, we described high-resolution, high-sensitivity SPIOs in nonpolar media[39] that exhibited optimal behavior at high concentrations and excitation amplitudes (Figure 1A–C, imaged in a 6.3 T/m FFL scanner[19]). In MPI scanners, these SPIOs (Figure 1D,E) showed a resolution 20-fold higher resolution than that shown in powder DC magnetometry (Figure 1F). Briefly, the thin ($\sim 2-3$ nm) coating allows these SPIOs to apply fields on neighboring SPIOs at higher concentrations (i.e., lower interparticle distances), effectively amplifying externally applied fields. This amplification increases as interparticle distance approaches one diameter, where the particles form chainlike mesostructures (Figure 1G).[40,41] Importantly, a simple, positive-feedback model using a Langevin operator yields a compelling magnetic model for these SPIOs (Figure 1H), predicting the observed hysteresis and PSF (Figure 1I). This ensemble regenerative magnetic response has previously been described in literature as superferromagnetism[42–44] but had not been examined in the context of inductive detection and magnetic particle imaging. We thus described these particles as superferromagnetic iron oxide nanoparticles (SFMIOs).

With the resolution improvements offered by SFMIOs, scanner field strengths could be $10\times$ weaker while maintaining MPI's current resolution in humans, allowing for up to a $100\times$ reduction in cost. However, while SFMIOs offer incredible benefits, their properties are highly dependent on the magnetically generated SFMIO chains[39] (Figure 1G), which have time-varying hysteresis, remanence, and coercivity. Assessing SFMIO characteristics to ensure safe and efficient SFMIO scans is thus essential for clinical translation for MPI. In this work, we characterize SFMIO remanence with a novel pulse sequence, assess SFMIO remanence decay and reformation after magnetic polarization, and propose future MPI scan strategies required to optimally and safely image SFMIOs.

~ 21 nm magnetite nanoparticles (SFMIOs) were synthesized via thermal decomposition[45] and suspended in hexane, with a thin oleic acid coating. 40 μL of SFMIOs at 2.76 mg Fe/mL (quantified by Perl's Prussian Blue reaction) were measured in an arbitrary-waveform relaxometer.[46] The point spread function (PSF) was measured using sinusoidal 20 kHz fields of amplitude $B_{\text{app}} = [1\ \text{mT},\ 10\ \text{mT}]$, to assess their resolution, coercivity, and signal. Notably, the SFMIOs demonstrated super-resolution behavior when the excitation amplitude B_{app} was greater than the coercivity threshold B_{th}, empirically determined as 4 mT (Figure 1D).

Standard MPI sequences utilize purely sinusoidal waveforms. Extracting remanence evolution from these excitation patterns would require deconvolution of effects of the constantly varying fields, greatly complicating any investigation. As such, a novel magnetic pulse sequence (reminiscent of pulsed MPI[25]) was devised to measure magnetic remanence, utilizing a home-built arbitrary-waveform relaxometer (Figure 2A).[46] We describe the measurement signal of remanence decay phenomenologically in eq 2

$$M(\text{TE}) = (M_{\text{pol}} - M_{\infty})\text{e}^{-TE/\tau_{\text{decay}}} + M_{\infty} \tag{2}$$

where M is the magnetization at time TE, M_{pol} is the magnetization of the fully polarized SPIO structure, TE is the echo time from an initial polarizing pulse to a readout pulse, τ_{decay} is the measured remanence decay constant, and M_{∞} is the steady-state magnetization, including any steady-state remanence.

The first-of-its-kind MPI multiecho sequence (Figure 2B) concatenates consecutive magnetic pulses with increasing echo time (TE) at 0 mT in order to measure the effective remanence decay behavior after polarization. Specifically, SFMIOs were polarized using strong fields ($B_{pol} = 30$ mT, $t_{pol} = 30$ s) and then measured with alternating trapezoidal pulses ($t_{rise} = 10$ μs, $t_{dur} = 3$ ms, $B_{Tx} = \pm 32$ mT) with increasing interpulse duration ($TE_i = [100$ μs, 80 ms]). The resultant signal (Figure 2C,D) represents remanence with an increasing echo time TE_i, providing a surrogate measurement of SFMIO remanence and its evolution during an MPI scan. Notably, this multiecho approach allows for inductive measurement of slow decay constants that provide minimal signal.

As shown in Figure 2D, the MPI signal of SFMIOs exponentially decayed with increasing TE at 0 mT field ($\tau_{decay} \approx 120$ ms) but did not fully lose super-resolution behavior. While the observed decay did not disrupt super-resolution behavior in standard scans, any variation in amplitude could confound intraimage analysis.

To dissect the effects of our multiecho sequence on SFMIO remanence, we examine its individual components. The prototypical sequence (shown in Figure 3A, top) traverses the SFMIO hysteresis curve (Figure 3A, bottom), first polarizing the sample (Figure 3A, i) and then allowing the sample to sit at 0 mT for some echo time TE (Figure 3A, ii,iii), then measuring the resultant remanence and consequent transition $M(TE) = M_{TE} + M_{sat}$ (Figure 3A, iv) as the sample repolarizes in the opposite direction.

To further characterize remanence evolution, various pulse sequence parameters were modified and the resultant decay pattern measured. To assess decay during nonzero fields, the same stock sample was measured while applying various steady-state fields ($B_{SS} = [-2$ mT, 0.5 mT]) (Figure 3B). Figure 3C shows the remanence evolution as a function of steady-state field for SFMIOs polarized in the negative direction ($M_{SFMIO} < 0$). When fields parallel to the structure ($B_{SS} < 0$) were applied, the SFMIO signal showed decreased or minimal decay. In comparison, applying minimal antiparallel fields ($B_{SS} > 0$) showed greatly accelerated decay with ($\tau_{decay} \approx 13$ ms) even at $B_{ss} = 0.5$ mT. This suggests that parallel fields can mitigate decay, depending on the strength of the reinforcing field.

In the excitation field in a standard MPI scan, SFMIO chains will mostly tend to experience reinforcing fields, with antiparallel fields occurring as the field sweeps past 0 mT to the coercive threshold opposing the SFMIO chain ($B_{coercivity} \approx \pm 4$ mT in Figure 3). Thus, the minimum scan speed for SFMIOs should be governed by the transition in this region. Given that the fastest decay was shorter than the sampling period (for B_{SS} approaching $B_{coercivity}$, in Supplemental Figure 2), the frequency threshold is only lower bound by our measurement (i.e., $dB/dt > B_{coercivity}/\min(\tau_{decay,meas}) = 15$ Hz). More generally, the minimum scan rate will be

$$\left(\frac{dB}{dt}\right)_{\min} \approx \frac{B_{\text{coercivity}}}{\bar{\tau}_{\text{decay}}} \tag{3}$$

$$\approx \frac{B_{\text{coercivity}}}{\left(\int_0^{B_{\text{coercivity}}} \tau_{\text{decay}}(B)\,dB\right)/B_{\text{coercivity}}} \tag{4}$$

assuming a constant slew rate. This accounts for all decay rates between 0 mT and $B_{\text{coercivity}}$. The derived lower bound is congruent with previous SFMIO measurements versus frequency, which showed super-resolution behavior above 100 Hz ($B_{\text{app}} = 20$ mT),[39] and sets limits for the SFMIO scan trajectory design.

To assess how quickly the SFMIO chains are reformed after perturbation, the echo ordering of the sequence was reversed (Figure 3D), and the pulse duration t_{dur} was varied from $t_{\text{dur}} = [1\text{ ms},\ 20\text{ ms}]$. The resultant signal is then a recursive composition of remanence decay and reformation

$$M(\text{TE}_i) = (M_{\text{pol}} - M_\infty)e^{-\text{TE}_i/\tau_{\text{decay}}} \left[1 - e^{-t_{\text{dur}}/\tau_{\text{ref}}}\left(1 - M(\text{TE}_{i-1})/M_{\text{pol}}\right)\right] + M_\infty \tag{5}$$

where τ_{ref} is a chain reformation constant, TE_i represents the ith echo time for a given ordering, and $M(\text{TE}_{i-1})$ represents the previous echo's signal for a given ordering. From this equation, pulse durations that are insufficient for full reformation (i.e., t_{dur} faster than τ_{ref}) should yield inconsistent measurements for varying echo orders, as contributions from initial measurements will appear in later echoes. However, for $t_{\text{dur}} \gg \tau_{\text{ref}}$, the term $\exp(-t_{\text{dur}}/\tau_{\text{ref}})$ (representing contributions from previous echoes) nears zero and eq 5 simplifies to eq 2.

The resultant decay patterns are shown in Figure 3E,F: for $t_{\text{dur}} < 10$ ms, the reverse sequences yield different measurements than forward sequences, visible as a nonmonotonic function of TE. In comparison, the decay patterns with consistent decay irrespective of delay order in Figure 3 imply full chain reformation for $t_{\text{dur}} \geq 10$ ms. This yields an estimate of $\tau_{\text{ref}} \approx 2$ ms, assuming that $5\tau_{\text{ref}}$ yields complete chain reformation.

Remanence decay and reformation can occur for various reasons. For one, the SFMIO chain could be an unstable colloid, dispersing at 0 mT and resulting in superparamagnetism.[50,51] Reformation would then be the complete reformation of the SFMIO chains. However, this seems unlikely on the basis of the potential energies for interacting particles. Consider two SPIOs with aligned domains (Figure 4A,B, top), under some magnetic field. Traditional DLVO models[47,48] for charge-separated ferrofluids[49,52] have two stable energy minima that can exist for these SPIOs (characteristic curve in Figure 4A, bottom) due to electrostatic

repulsion, van der Waals interactions, and magnetic attraction. Colloidal dispersion can then occur when the magnetic field is removed, and the secondary minima disappears.

However, for sterically hindered particles in nonpolar media (as in the experiments above), the electrostatic force from surface charge is insignificant and no secondary minima exists (Figure 4B, bottom). Steric hindrance prevents bulk matter formation at $\sim 2\delta$, where δ is the surface ligand's length.[53] In this case, colloidal dispersion is not energetically favorable. Theoretically, applying an opposing field equivalent to SFMIO coercivity could negate magnetic attraction momentarily, leaving only van der Waals interactions to stabilize the colloid. However, steady-state experiments (Figure 3C) showed that even small antiparallel fields (well below the coercivity) accelerate decay. Thus, the chains are likely not spontaneously breaking apart.

Instead, the SFMIO chains may simply be misaligned from the measurement axis. If left alone, individual particles may stick together, but the chains could point in different directions.[41] Previous work[39] has shown that SFMIO super-resolution behavior occurs only when the structure aligns with the measurement axis; if the chain is orthogonal to the measurement axis, the SFMIOs appear superparamagnetic. Similar hysteresis changes have been observed in cryomagnetometry of bionized nanoferrite.[54] A misalignment of the chains could allow for superferromagnetism, but with a reduced signal. Indeed, when the sample was measured after TE = 12 s (i.e., $\gg 5\tau_{decay}$), we continued to observe super-resolution behavior (Figure 4C, bottom) and visually saw SFMIO chaining. To ensure that the SFMIO chain was yielding steady-state superferromagnetism, the sample was mechanically agitated for 30 s at the same time point (TE = 12 s). As shown in Figure 4C, top, only superparamagnetic behavior remains. This hypothesis also accounts for decay acceleration in small, opposing fields, as antiparallel chains in a unidirectional field are in an unstable equilibrium, and any perturbation would result in magnetic torquing.[55]

We further tested this hypothesis by examining polarized SFMIOs after dilution and sonication. Even after 10-fold dilution, the SFMIOs maintained superferromagnetism (Figure 4D). If spontaneous dissolution was occurring, this diluted solution should not show superferromagnetic behavior, as the sample is below the concentration threshold for superferromagnetism.[39] The observation otherwise suggests that the chains are maintained, even through dilution. In comparison, sonication (Figure 4E) was able to return the sample to superparamagnetism, implying that the chains had been broken. As sonication imparts intense, localized energy through cavitation,[56] it is unlikely that the SFMIO chains could undergo this dissolution during MPI scans.

This steady-state remanence has implications for the encapsulation of SFMIOs for *in vivo* usage. SFMIOs currently show superferromagnetism in nonpolar solvents—we previously showed a 1% v/v Tween-20/Triton-X proof-of-concept encapsulation that allowed for solvation in water but had minimal stability.[39] Remanence decay provides another design criterion for encapsulation, given its apparent dependence on alignment to the measurement axis and container shape. As SFMIOs may require high bioavailability to have reasonable

clearance through the liver, encapsulation may require less stability. Future research will need to focus on assessing these trade-offs for optimal encapsulation.

To connect remanence and coercivity measurements toward optimal scans, another batch of SFMIOs (characterized in Supplemental Figure 3: $B_{th} = 8$ mT) were scanned in the relaxometer across various frequencies ($f = [100$ Hz, 10 kHz]) and amplitudes ($B_{app} = [1$ mT, 20 mT]). The peak SNR was optimized at high amplitudes, above a frequency threshold (Figure 5A, at $B_{app} = 20$ mT and $f \geq 1$ kHz). The sharp SNR drop-off below frequency and amplitude thresholds corroborates slew rate and coercivity thresholds for SFMIOs, as expected from our remanence decay measurements. The SNR optimum at high-amplitude suggests that MPI scan trajectories require a complete rework to best utilize SFMIOs. Given that SFMIO coercivity yields worse scan efficiency at lower amplitudes (Figure 5B), and MPI safety concerns set frequency limits for a fixed amplitude[57] (Figure 5C), it is clear that optimal SPIO scan strategies[35] (low-amplitude, high-frequency) are unusable for SFMIOs.

We propose a new scan that covers the full magnetic field of view per half-cycle: the Single Pass and Raster (SPaR) sequence (Figure 5D). The frequency would be lowered to accommodate MPI safety limits down to the limits specified by remanence decay. SPaR could be implemented in the transverse or longitudinal axis depending on scanner hardware limitations. Future work will focus on SPaR implementation and optimization at higher amplitudes (~ 99 mT for FOV $= 30$ cm, $G = 6.3$ T/m, and $B_{coercivity} = 8$ mT).

This work investigated the effects of SFMIO remanence and coercivity on MPI scanning. We found remanence decay and reformation to be dependent on applied magnetic fields. Optimal MPI scanning was found to be above the minimum excitation frequencies and at high amplitudes, yielding optimal SNR while maintaining their >10-fold resolution improvement. Remanence decay and coercivity thresholds bound these optimal scan parameters. We propose that further scanner development utilizes the Single Pass and Raster sequence, using high-amplitude, low-frequency excitation to safely and efficiently scan SFMIOs. The resolution improvements from SFMIOs could lead to 100-fold cheaper scanners and are crucial for the clinical translation of MPI.

Supplementary Material

Refer to Web version on PubMed Central for supplementary material.

ACKNOWLEDGMENTS

The authors thank the Salahuddin Lab (especially J. C. H. Hsu) at UC Berkeley for usage of their VSM; the Electron Microscopy Lab at UC Berkeley for usage of their equipment; and Z. W. Tay, X. Y. Zhou, and Q. L. Huynh for discussions.

Funding

The authors acknowledge support from NIH grants R01s EB024578, EB029822, T32 GM 098218, and R44 EB029877, UC TRDRP grant 26IP-0049, UC Discovery Award, M. Cook Chair, Bakar Fellowship, NSERC PGSD3-532656-2019 Fellowship, UCB Bioengineering Craven Fellowship, UC CRCC Doctoral Fellowship, Siebel Scholars program, and NSF GRFP.

REFERENCES

(1). Gleich B; Weizenecker J Tomographic imaging using the nonlinear response of magnetic particles. Nature 2005, 435, 1214–1217. [PubMed: 15988521]

(2). Goodwill PW; Saritas EU; Croft LR; Kim TN; Krishnan KM; Schaffer DV; Conolly SM X-Space MPI: Magnetic Nanoparticles for Safe Medical Imaging. Adv. Mater 2012, 24, 3870–3877. [PubMed: 22988557]

(3). Dias MHM; Lauterbur PC Ferromagnetic particles as contrast agents for magnetic resonance imaging of liver and spleen. Magn. Reson. Med 1986, 3, 328–330. [PubMed: 3713497]

(4). Song G; Zheng X; Wang Y; Xia X; Chu S; Rao J A Magneto-Optical Nanoplatform for Multimodality Imaging of Tumors in Mice. ACS Nano 2019, 13, 7750–7758. [PubMed: 31244043]

(5). Laurent S; Forge D; Port M; Roch A; Robic C; Vander Elst L; Muller RN Magnetic Iron Oxide Nanoparticles: Synthesis, Stabilization, Vectorization, Physicochemical Characterizations, and Biological Applications. Chem. Rev 2008, 108, 2064–2110. [PubMed: 18543879]

(6). Corot C; Robert P; Idée J-M; Port M Recent advances in iron oxide nanocrystal technology for medical imaging. Adv. Drug Delivery Rev 2006, 58, 1471–1504. Particulate Nanomedicines.

(7). Schenck JF The role of magnetic susceptibility in magnetic resonance imaging: MRI magnetic compatibility of hte first and second kinds. Medical Physics 1996, 23, 815–850. [PubMed: 8798169]

(8). Cunningham CH; Arai T; Yang PC; McConnell MV; Pauly JM; Conolly SM Positive contrast magnetic resonance imaging of cells labeled with magnetic nanoparticles. Magn. Reson. Med 2005, 53, 999–1005. [PubMed: 15844142]

(9). Stueber DD; Villanova J; Aponte I; Xiao Z; Colvin VL Magnetic Nanoparticles in Biology and Medicine: Past, Present, and Future Trends. Pharmaceutics 2021, 13, 943. [PubMed: 34202604]

(10). Reimer P; Tombach B Hepatic MRI with : detection and characterization of focal liver lesions. European Radiology 1998, 8, 1198–1204. [PubMed: 9724439]

(11). Bean CP Hysteresis Loops of Mixtures of Ferromagnetic Micropowders. J. Appl. Phys 1955, 26, 1381–1383.

(12). Rahmer J; Weizenecker J; Gleich B; Borgert J Signal encoding in magnetic particle imaging: Properties of the system function. BMC Medical Imaging 2009, 9, 1–21. [PubMed: 19133127]

(13). Saritas EU; Goodwill PW; Croft LR; Konkle JJ; Lu K; Zheng B; Conolly SM Magnetic Particle Imaging (MPI) for NMR and MRI researchers. J. Magn. Reson 2013, 229, 116–126. [PubMed: 23305842]

(14). Goodwill PW; Lu K; Zheng B; Conolly SM An x-space magnetic particle imaging scanner. Rev. Sci. Instrum 2012, 83, 033708. [PubMed: 22462930]

(15). Zhou XY; Jeffris KE; Yu EY; Zheng B; Goodwill PW; Nahid P; Conolly SM First in vivo magnetic particle imaging of lung perfusion in rats. Phys. Med. Biol 2017, 62, 3510–3522. [PubMed: 28218614]

(16). Zhou XY; Tay ZW; Chandrasekharan P; Yu EY; Hensley DW; Orendorff R; Jeffris KE; Mai D; Zheng B; Goodwill PW; Conolly SM Magnetic particle imaging for radiation-free, sensitive and high-contrast vascular imaging and cell tracking. Curr. Opin. Chem. Biol 2018, 45, 131–138. [PubMed: 29754007]

(17). Tay ZW; Chandrasekharan P; Zhou XY; Yu E; Zheng B; Conolly S In vivo tracking and quantification of inhaled aerosol using magnetic particle imaging towards inhaled therapeutic monitoring. Theranostics 2018, 8, 3676–3687. [PubMed: 30026874]

(18). Yu EY; Bishop M; Zheng B; Ferguson RM; Khandhar AP; Kemp SJ; Krishnan KM; Goodwill PW; Conolly SM Magnetic Particle Imaging: A Novel in Vivo Imaging Platform for Cancer Detection. Nano Lett 2017, 17, 1648–1654. [PubMed: 28206771]

(19). Yu EY; Chandrasekharan P; Berzon R; Tay ZW; Zhou XY; Khandhar AP; Ferguson RM; Kemp SJ; Zheng B; Goodwill PW; Wendland MF; Krishnan KM; Behr S; Carter J; Conolly SM Magnetic Particle Imaging for Highly Sensitive, Quantitative, and Safe in Vivo Gut Bleed Detection in a Murine Model. ACS Nano 2017, 11, 12067–12076. [PubMed: 29165995]

(20). Gaudet JM; Makela AV; Foster PJ Chain Formation is essential for Super-Resolution MPI. Proceedings of the American Association for Cancer Research Annual Meeting 2019, 79, 1138.

(21). Chandrasekharan P; et al. Non-radioactive and sensitive tracking of neutrophils towards inflammation using antibody functionalized magnetic particle imaging tracers. Nanotheranostics 2021, 5, 240–255. [PubMed: 33614400]

(22). Zhu X; Li J; Peng P; Hosseini Nassab N; Smith BR Quantitative Drug Release Monitoring in Tumors of Living Subjects by Magnetic Particle Imaging Nanocomposite. Nano Lett 2019, 19, 6725–6733. [PubMed: 31498999]

(23). Gevaert JJ; Fink C; Dikeakos JD; Dekaban GA; Foster PJ Magnetic Particle Imaging Is a Sensitive In Vivo Imaging Modality for the Detection of Dendritic Cell Migration. Molecular Imaging and Biology 2022, 24, 886–897. [PubMed: 35648316]

(24). Wang P; Goodwill PW; Pandit P; Gaudet J; Ross A; Wang J; Yu E; Hensley DW; Doyl TC; Contag CH; Conolly S; Moore A Magnetic particle imaging of islet transplantation in the liver and under the kidney capsule in mouse models. Quantitative Imaging in Medicine and Surgery 2018, 8, 114–122. [PubMed: 29675353]

(25). Tay ZW; Hensley D; Ma J; Chandrasekharan P; Zheng B; Goodwill P; Conolly S Pulsed Excitation in Magnetic Particle Imaging. IEEE Transactions on Medical Imaging 2019, 38, 2389–2399. [PubMed: 30762537]

(26). Hensley D; Tay ZW; Dhavalikar R; Zheng B; Goodwill P; Rinaldi C; Conolly S Combining magnetic particle imaging and magnetic fluid hyperthermia in a theranostic platform. Phys. Med. Biol 2017, 62, 3483–3500. [PubMed: 28032621]

(27). Chandrasekharan P; et al. Using magnetic particle imaging systems to localize and guide magnetic hyperthermia treatment: tracers, hardware, and future medical applications. Theranostics 2020, 10, 2965–2981. [PubMed: 32194849]

(28). Tay ZW; Hensley DW; Vreeland EC; Zheng B; Conolly SM The relaxation wall: experimental limits to improving MPI spatial resolution by increasing nanoparticle core size. Biomedical Physics & Engineering Express 2017, 3, 035003. [PubMed: 29250434]

(29). Goodwill P; Croft L; Konkle J; Lu K; Saritas E; Zheng B; Conolly S Third Generation X-Space MPI Mouse and Rat Scanner. Magnetic Particle Imaging Berlin, Heidelberg 2012, 140, 261–265.

(30). Murase K; Hiratsuka S; Song R; Takeuchi Y Development of a system for magnetic particle imaging using neodymium magnets and gradiometer. Jpn. J. Appl. Phys 2014, 53, 067001.

(31). Yang Y; Bec J; Zhou J; Zhang M; Judenhofer MS; Bai X; Di K; Wu Y; Rodriguez M; Dokhale P; Shah KS; Farrell R; Qi J; Cherry SR A Prototype High-Resolution Small-Animal PET Scanner Dedicated to Mouse Brain Imaging. J. Nucl. Med 2016, 57, 1130–1135. [PubMed: 27013696]

(32). Croft LR; Goodwill PW; Conolly SM Relaxation in X-Space Magnetic Particle Imaging. IEEE Transactions on Medical Imaging 2012, 31, 2335–2342. [PubMed: 22968211]

(33). Montgomery DB Solenoid magnet design: The magnetic and mechanical aspects of resistive and superconducting systems; Wiley-Interscience, 1868.

(34). Rosensweig R Heating magnetic fluid with alternating magnetic field. J. Magn. Magn. Mater 2002, 252, 370–374.

(35). Tay ZW; Hensley DW; Chandrasekharan P; Zheng B; Conolly SM Optimization of Drive Parameters for Resolution, Sensitivity and Safety in Magnetic Particle Imaging. IEEE Transactions on Medical Imaging 2020, 39, 1724–1734. [PubMed: 31796392]

(36). Croft LR; Goodwill PW; Konkle JJ; Arami H; Price DA; Li AX; Saritas EU; Conolly SM Low drive field amplitude for improved image resolution in magnetic particle imaging. Medical Physics 2016, 43, 424–435. [PubMed: 26745935]

(37). Dittmer S; Kluth T; Baguer DO; Maass P A Deep Prior Approach to Magnetic Particle Imaging. Machine Learning for Medical Image Reconstruction Cham 2020, 12450, 113–122.

(38). Lieb F; Knopp T A wavelet-based sparse row-action method for image reconstruction in magnetic particle imaging. Medical Physics 2021, 48, 3893–3903. [PubMed: 33982810]

(39). Tay ZW; Savliwala S; Hensley DW; Fung KLB; Colson C; Fellows BD; Zhou XY; Huynh Q; Lu Y; Zheng B; Chandrasekharan P; Rivera-Jimenez S; Conolly SM Superferromagnetic Nanoparticles enable Order-of-magnitude Resolution and Sensitivity Gain in Magnetic Particle Imaging. Small Materials 2021, 5, 2100796.

(40). Colson C; Fung KLB; Bryan J; Tay ZW; Fellows BD; Saayuja C; Kuo R; Chandrasekharan P; Conolly SM Evidence that Chain Formation is Essential for High-Resolution MPI. bioRxiv 2022, DOI: 10.1101/2022.11.27.518061.

(41). Butter K; Bomans PH; Frederik PM; Vroege GJ; Philipse AP Direct observation of dipolar chains in ferrofluids in zero field using cryogenic electron microscopy. J. Phys.: Condens. Matter 2003, 15, S1451–S1470.

(42). Bostanjoglo O; Röhkel K Superferromagnetism in thin Gd and Gd-Au films. Physica Status Solidi (a) 1971, 7, 387–392.

(43). Mørup S; Christiansen G Influence of magnetic anisotropy on the superferromagnetic ordering in nanocomposites. J. Appl. Phys 1993, 73, 6955–6957.

(44). Mørup S Superferromagnetic nanostructures. Hyperfine Interact 1994, 90, 171–185.

(45). Vreeland EC; Watt J; Schober GB; Hance BG; Austin MJ; Price AD; Fellows BD; Monson TC; Hudak NS; Maldonado-Camargo L; Bohorquez AC; Rinaldi C; Huber DL Enhanced Nanoparticle Size Control by Extending LaMer's Mechanism. Chem. Mater 2015, 27, 6059–6066.

(46). Tay ZW; Goodwill PW; Hensley DW; Taylor LA; Zheng B; Conolly SM A High-Throughput, Arbitrary-Waveform, MPI Spectrometer and Relaxometer for Comprehensive Magnetic Particle Optimization and Characterization. Sci. Rep 2016, 6, 34180. [PubMed: 27686629]

(47). Derjaguin B; Landau L Acta Physicochim. URSS 1941, 14, 633.

(48). Verwey EJW; Overbeek JTG Theory of the stability of lyophobic colloids. Journal of Colloid Science 1955, 10, 224–225.

(49). Faraudo J; Andreu JS; Camacho J Understanding diluted dispersions of superparamagnetic particles under strong magnetic fields: A review of concepts, theory and simulations. Soft Matter 2013, 9, 6654–6664.

(50). Laskar JM; Philip J; Raj B Experimental evidence for reversible zippering of chains in magnetic nanofluids under external magnetic fields. Physical Review E - Statistical, Nonlinear, and Soft Matter Physics 2009, 80, 1–8.

(51). Hayes CF; Hwang SR Observation of magnetically induced polarization in a ferrofluid. J. Colloid Interface Sci 1977, 60, 443–447.

(52). Martínez-Pedrero F; Tirado-Miranda M; Schmitt A; Callejas-Fernández J Primary and secondary bonds in field induced aggregation of electric double layered magnetic particles. Langmuir 2009, 25, 6658–6664. [PubMed: 19453108]

(53). Di Marco M; Sadun C; Port M; Guilbert I; Couvreur P; Dubernet C Physicochemical characterization of ultrasmall superparamagnetic iron oxide particles (USPIO) for biomedical application as MRI contrast agents. Int. J. Nanomed 2007, 2, 609–622.

(54). Boekelheide Z; Miller JT; Grüttner C; Dennis CL The effects of intraparticle structure and interparticle interactions on the magnetic hysteresis loop of magnetic nanoparticles. J. Appl. Phys 2019, 126, 043903.

(55). Cardoso VF; Francesko A; Ribeiro C; Banobre-López M; Martins P; Lanceros-Mendez S Advances in Magnetic Nanoparticles for Biomedical Applications. Adv. Healthcare Mater 2018, 7, 1700845.

(56). Wu P; Bai L; Lin W On the definition of cavitation intensity. Ultrasonics Sonochemistry 2020, 67, 105141. [PubMed: 32464502]

(57). Saritas EU; Goodwill PW; Zhang GZ; Conolly SM Magnetostimulation Limits in Magnetic Particle Imaging. IEEE Transactions on Medical Imaging 2013, 32, 1600–1610. [PubMed: 23649181]

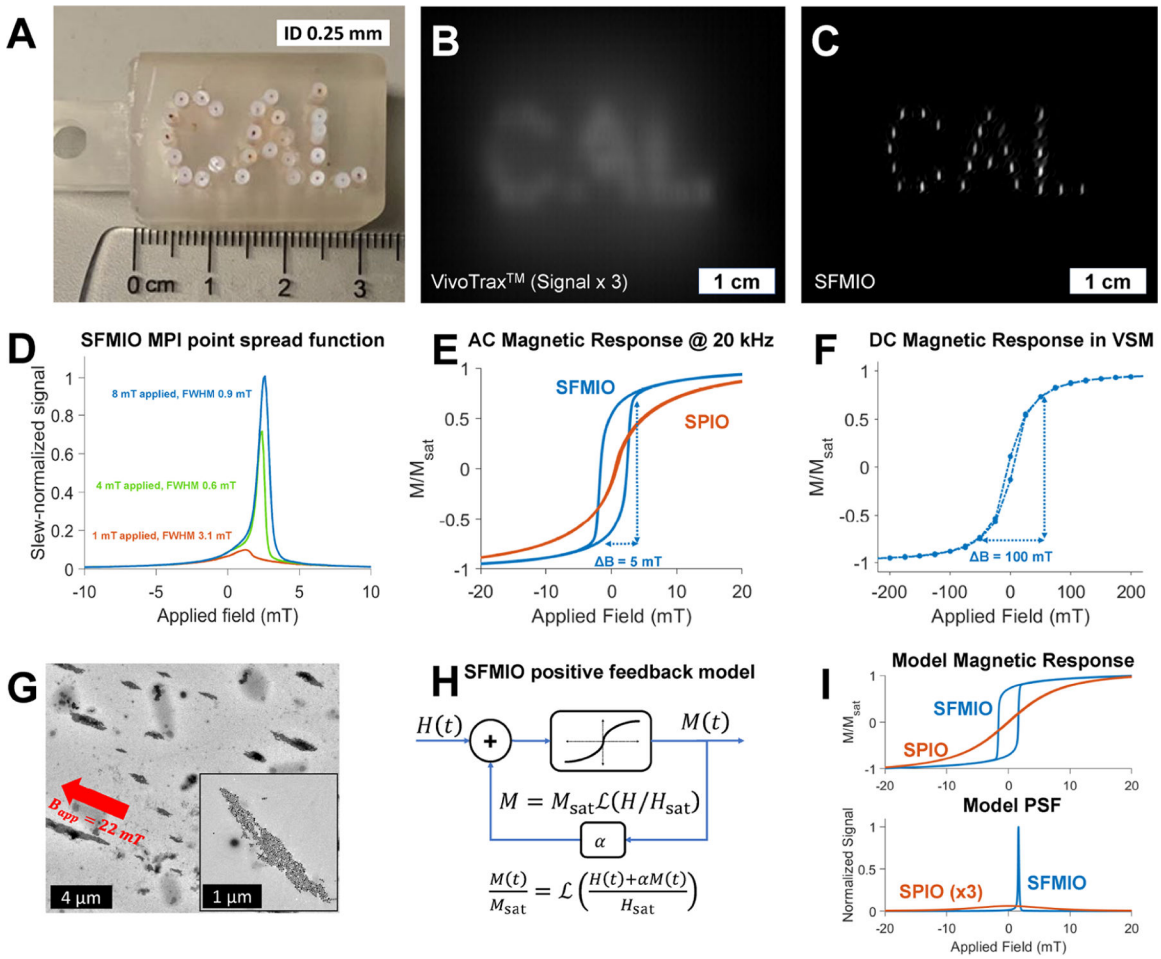

Figure 1.

SFMIOs show 10-fold resolution in MPI. Recent single-core magnetite iron oxide nanoparticles, dubbed superferromagnetic iron oxide particles (SFMIOs) show 10-fold resolution improvement compared to ferrucarbotran (A–C). When these particles are at high concentration and are excited with a strong magnetic field, their peak signal and resolution greatly improve (D). These particles show strong hysteresis and sharp magnetic transitions (E) in MPI scanners in solution, but dried samples measured in a Lake Shore Cryotronics 7400 series vibrating sample magnetometer (VSM) show superparamagnetic behavior (F). This resolution improvement is hypothesized to be due to particle–particle interactions, which are possible thanks to the size of the particles (21–30 nm[39,40]) vs their coating (~ 1 nm). These particles appear to form chainlike structures when dried under a field (visualized under electron microscopy) (G, adapted with permission from ref 39. Copyright 2021 Wiley-VCH GmbH). Indeed, a simple positive-feedback model (H), using the Langevin function as the system function, yields a magnetic response (I) that shows nearly identical behavior, lending credence to the hypothesis.

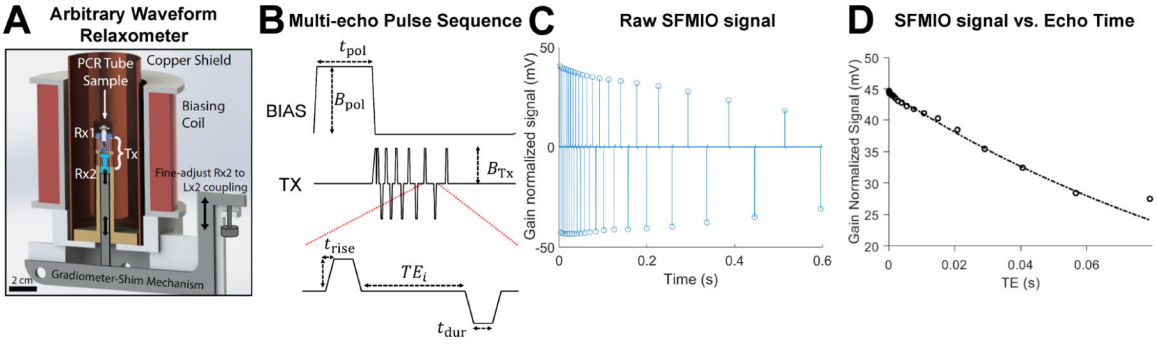

Figure 2.

Measuring SFMIO remanence and remanence evolution. To measure the relatively slow variation in SFMIO remanence, we utilized an arbitrary wave relaxometer (A, reproduced with permission from ref 46. Copyright 2016 Tay et al. under CC BY 4.0) to apply an arbitrary magnetic pulse sequence with minimal feedthrough. The pulse sequence (B) first polarizes the SFMIOs to form chains with a large (B_{pol}) and prolonged (t_{pol}) magnetic pulse using a high-inductance, high efficiency bias coil. It then reads out remanence decay by applying faster trapezoidal pulses (defined by rise time t_{rise}, pulse duration t_{dur}, and magnetic pulse amplitude B_{Tx}) with increasing interpulse spacing, dubbed echo times (TE, or TE_i for the spacing before the ith echo), to perform a multiecho readout, the first-of-its-kind in MPI. This latter set of magnetic pulses is performed with a responsive, lower inductance transmit (Tx) coil and allows inductive readout of slower decay constants. The raw signal (shown for the 40 μL SFMIO sample in (C)) can then be used to extract a function of SFMIO signal versus TE as a surrogate for SFMIO remanence (D), which yielded a remanence decay constant at zero field of $\tau_{decay}(B)|_{B=0} \approx 120$ ms.

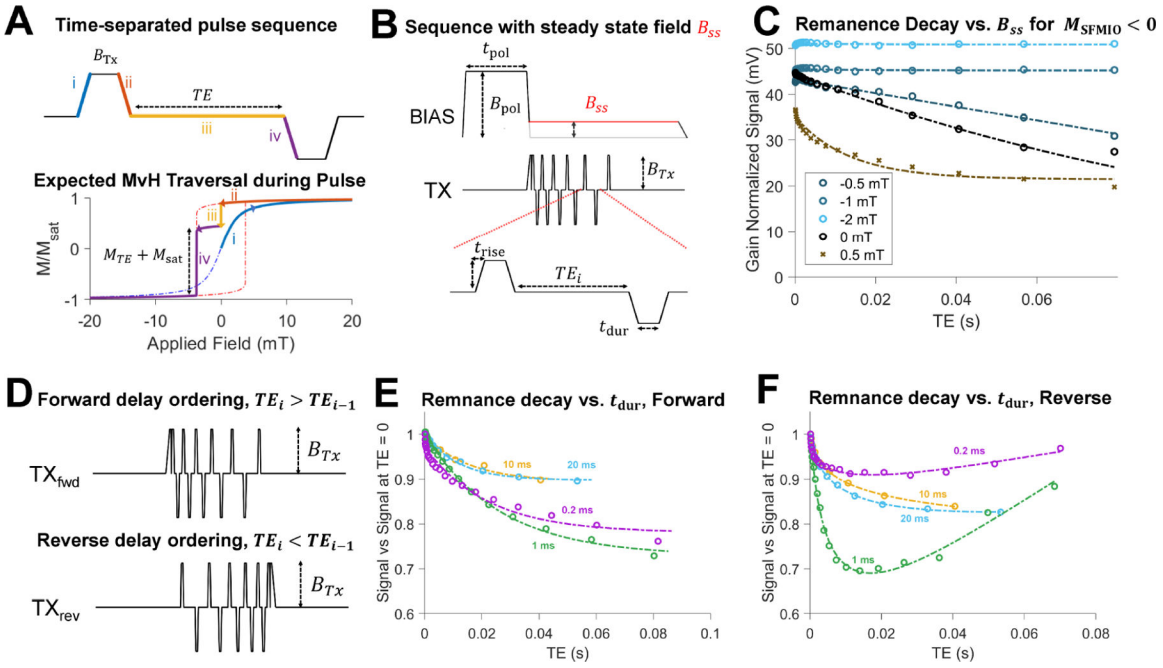

Figure 3.

Characterizing remanence decay in MPI scans and chain reformation. Our time- separated magnetic pulses (A, top) allow us to characterize the behavior of SFMIO remanence over time. Specifically, by polarizing the SFMIOs from Figure 2 with a pulse of amplitude B_{Tx} (i, ii) and allowing the sample to sit at zero field for some specified echo time TE (iii), we can read out using a secondary pulse to measure an MPI signal (iv) while also simultaneously repolarizing the particles. If we examine the traversal of the magnetic response curve (A, bottom), it is clear that this signal is a function of the remaining magnetization, $M_{\mathrm{TE}} + M_{\mathrm{sat}}$. (B) By modifying the multipulse sequence to have a steady-state field B_{SS} during acquisition, we altered the field at which remanence decay (A, iii) occurs. The decay mechanics for our sample at various fields is shown in (C). Notably, for a chain polarized in the negative direction ($M_{\mathrm{SPIO}} < 0$, small, antiparallel fields showed the acceleration of decay ($B_{\mathrm{SS}} > 0$, yellow), while parallel fields ($B_{\mathrm{SS}} < 0$, blue) showed reinforcement and decay suppression. Similar relationships were observed for chains polarized in the opposite directions. By modifying the delay order (D), we could see the effect of echo-ordering and provide an estimate for the time constant for reformation after decay. For pulse lengths t_{dur} less than 10 ms, echo ordering produced wildly different decay patterns (E, F), while pulse lengths equal to or longer than 10 ms showed similar patterns (with lines as guides for the eyes). This leads to an estimate for $5\tau_{\mathrm{ref}} = 10$ ms, assuming that 5 time constants are sufficient for steady-state reformation.

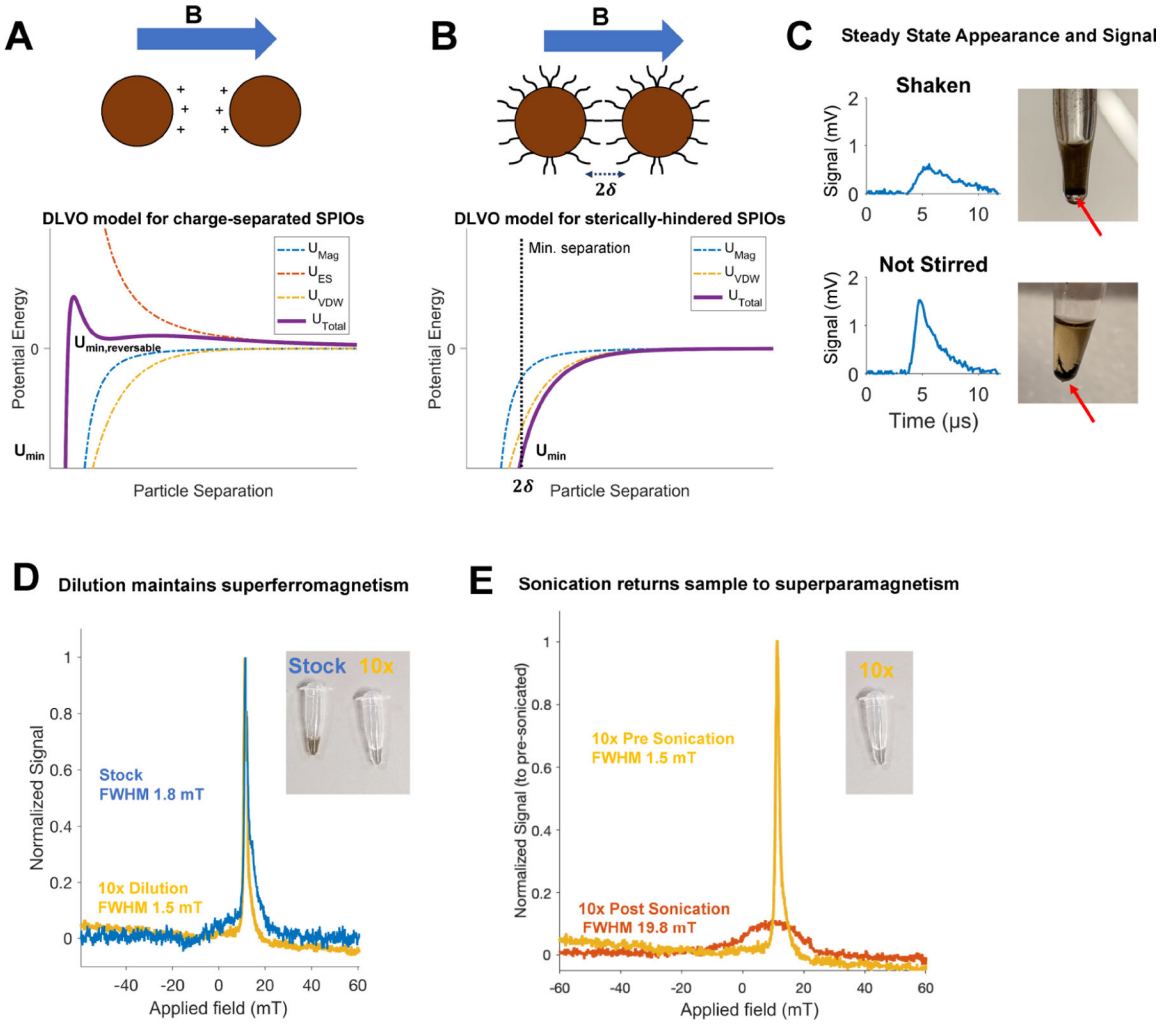

Figure 4.

Potential mechanisms for SFMIO remanence decay. Models of colloid stability provide insight into SFMIO remanence. While traditional ferrofluid theory has shown spontaneous dissolution, this was for charge-separated particles in aqueous media. For these cases, DLVO theory[47–49] (A) states that the potential for electrostatic repulsion, magnetic attraction, and van der Waals attraction governs colloidal stability. Specifically, the attractive and repulsive forces can allow for unstable aggregation in charge-separated SPIOs in specific configurations. However, sterically hindered SPIOs in nonpolar media (as in this work) show a single, irreversible minima caused by both attractive forces (B). As such, it is unlikely that spontaneous dissolution of the SFMIO chains is occurring. At steady state ($t = 12$ s, $t \gg 5\tau_{decay}$) with manual agitation for 30s, the sample showed standard SPIO behavior magnetically (C, top), with the SFMIOs visibly settling (as shown by the arrow). Conversely, for samples that were not shaken (or stirred) at steady-state (C, bottom), visual and magnetic inspection showed persistent chains and super-resolution activity. This was further confirmed by dilution of polarized SFMIOs, which maintained their super-resolution behavior (D), until after sonication (E).

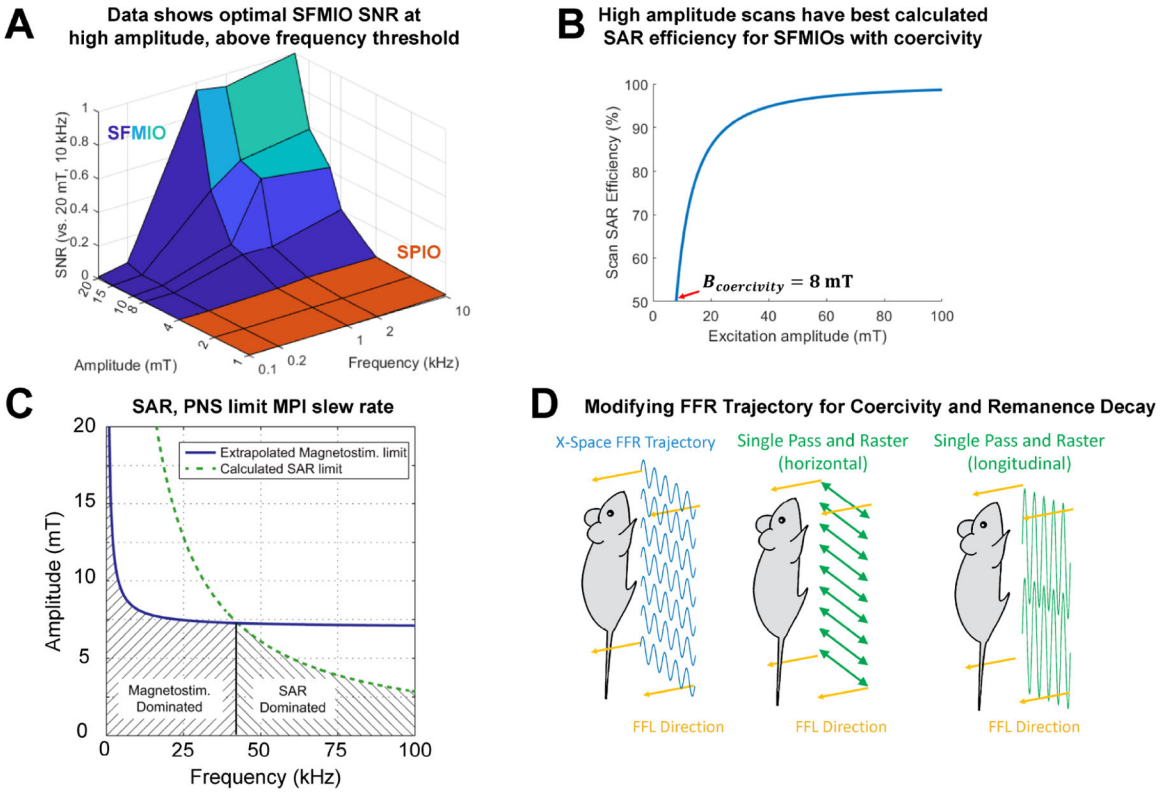

Figure 5.

Optimal MPI scanning with remanence decay and coercivity. The coercivity and remanence decay associated with SFMIOs alter what constitutes an optimal MPI scan. (A) A parametric sweep across frequency and amplitude shows that optimal SNR efficiency is at high amplitudes ($B_{app} = 20$ mT) and above a frequency threshold ($f \geq 1$ kHz). This sweep reveals the effects of both coercivity and remanence decay, showing extremely low SNR below frequency and amplitude thresholds. (B) Coercivity also lowers scan efficiency and unnecessarily heats subjects in lower amplitude scans, pointing toward high amplitude scans. (C) MPI is governed by magnetostimulation and specific absorption ratio (SAR) limits and requires scan parameters to be under frequency/amplitude thresholds. Adapted with permission from ref 57. Copyright 2013 IEEE. (D) Traditional MPI trajectories utilize 20 mT, 20 kHz acquisition, running into the aforementioned safety and efficiency concerns. This can be mitigated by increasing scan amplitudes and lowering excitation frequency to the limits specified by remanence decay. Taken to the limit, we propose the Single Pass and Raster (SPaR) sequence, which acquires the entire field of view (FOV) in a single half-cycle ($B_{app} = 99$ mT for $G = 6.3$ Tm^{-1}, FOV = 30 cm, $B_{coercivity} = 8$ mT), and lowers scan frequencies to the limit specified by remanence decay ($f = 1$ kHz). Note that the magnetic field of view may not cover the subject in the axial direction, necessitating mechanical translation.